Catalysis Communications 169 (2022) 106480

Contents lists available at ScienceDirect

Catalysis Communications

journal homepage: www.elsevier.com/locate/catcom

Facile synthesis of a porous 3D g-C_3N_4 photocatalyst for the degradation of organics in shale gas brines

Graham J. Hutchings, Philip R. Davies, Samuel Pattisson, Thomas E. Davies, David J. Morgan, Mbongiseni W. Dlamini *

Max Planck-Cardiff Centre on the Fundamentals of Heterogeneous Catalysis FUNCAT, Cardiff Catalysis Institute, School of Chemistry, Cardiff University, Main Building, Park Place, Cardiff, CF10 3AT, United Kingdom

ARTICLE INFO

Keywords:
Photocatalysis
Shale gas brines
Carbon nitride
3D photocatalysts
Water treatment
Produced water

ABSTRACT

Treatment and subsequent re-use of wastewater from shale gas extraction is a feasible strategy to ensure sustainability and reduce the environmental impact of the process. Here we demonstrate the photocatalytic benefits of improved three-dimensional graphitic carbon nitride (3D g-C_3N_4) during the degradation of organic contaminants. We show that precursor ratio (melamine to cyanuric acid) affects both the properties of 3D g-C_3N_4 as well as catalytic performance. When optimized, 3D g-C_3N_4 displayed the highest organics removal rate in brine-free solutions, achieving 99% conversion within 240 min. Significantly, the 3D g-C_3N_4 materials improved photocatalytic activity even in simulated shale gas brine solutions.

1. Introduction

Shale gas extraction has been increasing mainly because it is now considered the key bridging fuel to transition to renewable energy sources [1]. Shale gas has a much lower environmental footprint as an energy source, only producing 45% of CO_2 relative to coal [2,3]. Concerns still remain however about the large volumes of wastewater from shale gas extraction (called produced water) because it is a complex type of effluent shown to contain a range of organics, salts, minerals and metals, together with a high load of solids, including total dissolved solids, dissolved gases and microorganisms [4]. Owing to environmental concerns caused by produced water, much attention has been devoted to identifying a robust water treatment approach for such briny effluents. Semiconductor photocatalysis has great potential in resolving the dual challenge of water scarcity and water pollution caused by shale gas extraction. To achieve this target, a suitable photocatalyst with sufficient light harvesting properties, efficient separation of the photoinduced charge carriers and the generation of chloride-tolerant reactive oxygen species (ROS) is desirable.

As a semiconductor photocatalyst, graphitic carbon nitride (g-C_3N_4) has attracted research attention because it is visible-light active, chemically stable, non-toxic, can be synthesized from abundant and low-cost precursors, and possesses quite negative conduction band (CB) allowing for strong redox ability [5]. In addition, g-C_3N_4 has been reported to generate singlet oxygen ($^1O_2$) ROS upon photoexcitation [6]. Although it has a low reduction potential [$E^\circ(^1O_2/O_2^{\bullet-}) = +0.81\ V_{NHE}$], $^1O_2$ is a useful environmental oxidant because of its longer lifespan (4 μs) relative to $^\bullet OH$ radicals (1 ns) and is less susceptible to be scavenged by background ions in complex wastewater matrixes [7,8]. However, widespread application of bulk g-C_3N_4 is limited by several shortcomings such as a low specific surface area (10 m^2/g) and fast electron-hole recombination rate [9]. Recently, three-dimensional carbon nitride (3D g-C_3N_4) has been prepared and shown to prevent agglomeration of the nanosheets and consequently improved water splitting achieving an apparent quantum yield (AQY) as high as 1.4% under visible light [10]. Inspired by the unique properties of g-C_3N_4, we aimed to address the low surface area of g-C_3N_4 and test whether the prepared porous materials are better at resisting chloride poisoning during the photocatalytic treatment of organics in simulated shale gas brines.

2. Experimental

2.1. Synthesis of bulk and 3D g-C3N4

To prepare bulk g-C_3N_4, melamine (4 g) was transferred into a covered crucible and heated in a furnace at 550 °C (4 h, 5 °C/min). The final product was ground to a fine powder before use. 3D g-C_3N_4 was synthesized by the high temperature polymerization reaction of

* Corresponding author.
E-mail address: DlaminiM@cardiff.ac.uk (M.W. Dlamini).

https://doi.org/10.1016/j.catcom.2022.106480
Received 30 March 2022; Received in revised form 8 June 2022; Accepted 9 July 2022
Available online 14 July 2022

cyanuric acid-melamine supramolecular assemblies as reported elsewhere with slight modifications [10,11]. Typically, appropriate quantities of melamine and cyanuric acid (1,3,5-triazine-2,4,6-triol) were mixed in 50 mL deionized water and stirred at room temperature for 12 h to make cyanuric acid-melamine supramoleculars. The cyanuric acid-melamine supramoleculars were obtained by centrifugation and were purified by washing with ethanol and deionized water. Subsequently, the washed product was freeze-dried, ground to a fine powder and calcined at 550 °C (4 h, 5 °C/min) in a furnace.

2.2. Characterisation methods

N_2 sorption measurements were carried out on a Micromeritics 3Flex and Quantachrome Quadrasorb analysers. XRD characterizations were performed on a Philips X'Pert diffractometer fitted with Cu Kα radiation (λ = 1.54178 Å). UV–Vis diffuse reflectance spectroscopy (DRS) data was measured on an Agilent Cary 60 spectrophotometer using $BaSO_4$ as a reference material. The surface morphology was characterized using a field emission scanning electron microscope (Tescan MAIA3 Triglav FEG-SEM). Samples were coated with 10 nm 80:20 AuPd using a Quorum 150 TES sputter coater prior to SEM analysis. XPS analysis was done using a Thermo Scientific K-alpha+ spectrometer using a monochromatic Al Kα excitation source operated at 72 W and 1486.6 eV. The XPS data were fitted using CasaXPS software package (version 2.3.24) [12].

2.3. Photocatalytic tests

Photocatalytic experiments were performed in a double-walled open-top reactor with 110 mL of phenol aqueous solution (10 mg/L) used as the model organic compound. A Xe arc lamp (300 W, 1000 Wm^{-2}) was used as a light source and the catalyst concentration was maintained at 1 g/L. Before irradiation, the photocatalyst-phenol solution was stirred for 30 min in the dark to reach an absorption-desorption equilibrium. Sample aliquots (2 mL) were withdrawn at specific time intervals during photocatalytic experiments and analysed by a step-wise gradient elution HPLC method and by UV–Vis spectroscopy. Photocatalytic experiments were also performed in NaCl solutions (100 g/L Cl^-) to simulate shale gas brines, while the phenol and photocatalyst concentrations were maintained.

3. Results and discussion

We prepared 3D g-C_3N_4 with mol ratios of 2:1 and 1:1 melamine to cyanuric acid, in addition to bulk g-C_3N_4. Properties of bulk and 3D g-C_3N_4 materials were characterized by BET, XRD UV–Vis DRS, SEM and XPS analysis. Fig. 1a compares the adsorption and desorption isotherms of bulk and 3D g-C_3N_4 (2:1). The 3D g-C_3N_4 has a higher surface area (59

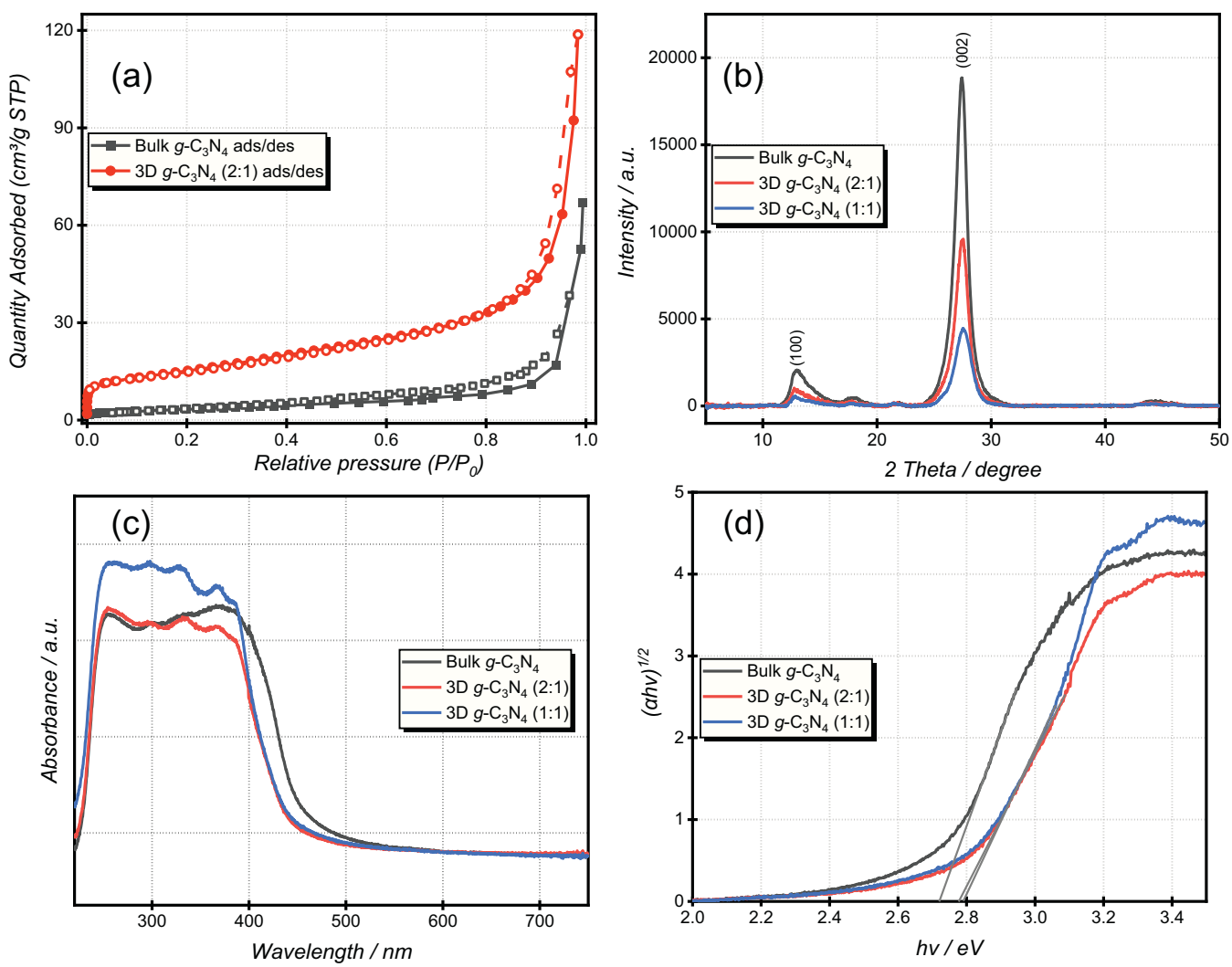

Fig. 1. (a) Adsorption-desorption isotherms of the samples, (b) XRD patterns and (c) UV–Vis DRS of the bulk and 3D g-C_3N_4 samples. (d) Tauc plots calculated from UV–Vis DRS results.

m^2/g) than bulk g-C_3N_4 (10 m^2/g). The isotherms are characterized as a type IV with an H3 hysteresis loop, which typically indicates the presence of mesopores along with some micropores.

X-ray diffraction (XRD) patterns were recorded to probe the phase structure of the three prepared g-C_3N_4 samples (Fig. 1b). All three XRD patterns exhibit two diffraction peaks at 13.1° and 27.4°, corresponding to the characteristic (100) and (002) planes of g-C_3N_4 which are assigned to the periodic stacking of tri-*s*-triazine rings and in-plane structural packing motif [13,14], respectively. The similarity of the (100) and (002) peak positions between samples suggests that the bulk structure of all three materials is similar and cyanuric acid addition does not influence the g-C_3N_4 formation mechanism. It is noted that the intensity of the peaks decreased corresponding to the amount of cyanuric acid used in the synthesis. This is because the 3D g-C_3N_4 (1:1) sample was more porous and fluffy [11,15], therefore a much smaller weight was required for a similar volume as the non-porous samples. Optical properties of the prepared samples were recorded by UV–Vis DRS and are displayed in Fig. 1c. A strong absorption band in the region 250–435 nm characteristic of g-C_3N_4 was observed in all the samples [16,17], with the bulk carbon nitride signal being slightly redshifted relative to the 3D g-C_3N_4 bands. The band gap energy of the g-C_3N_4 materials were estimated by the Tauc plot method. Bulk g-C_3N_4 has a band gap of 2.72 eV while that of 3D g-C_3N_4 is 2.78 and 2.79 eV for the 2:1 and 1:1 ratio samples respectively (Fig. 1d).

Fig. 2 compares SEM images of the bulk and 3D g-C_3N_4 (1:1) samples at the same scale to investigate their morphology and microstructure. Bulk g-C_3N_4 consisted of large solid agglomerates of stacked flakes (Fig. 2 a). The 3D g-C_3N_4 presented a coral-like morphology with an interconnected network of large pores (Fig. 2 c). Smaller open pores or voids of approximately 50–100 nm are also apparent across the surface. This was consistent with the low surface area BET measurements over the bulk g-C_3N_4 sample (10 m^2/g) and the high surface area measured on the porous 3D g-C_3N_4 (1:1) sample. This increase in porosity would lead to the improved transport and enhanced proximity of the reactants to the active areas of the catalyst surface. It would be expected that the improved dispersion of the catalyst through the liquid phase and greater exposure of the catalyst surface to irradiation would also enhance activity. The 3D g-C_3N_4 (2:1) sample is characterized by the presence of pores throughout the material (Fig. S1) but is generally more compact than the 3D g-C_3N_4 (1:1) material. The morphologies of 3D g-C_3N_4 confirm that cyanuric acid-melamine supramoleculars are an excellent precursor for porous graphitic carbon nitride as they minimize restacking of the nanosheets.

Surface analysis by XPS confirmed that the sample surfaces were mainly composed of carbon and nitrogen with residual oxygen also detected as shown by the survey spectra in Fig. S2. The bulk and 3D g-C_3N_4 samples had similar C and N compositions of 42% and 57% (Table S1) and the O content was less than 1% for all samples. High resolution C 1 s spectra (Fig. 3a) was deconvoluted into six peaks ascribed to adventitious carbon (284.7 eV), C–OH (286.6 eV), C–N–C (288 eV) and satellite peaks (293.4, 295.9, 299.1 and 300.2 eV) [18,19]. Table S2 summarizes the percentage compositions of the C 1 s spectra for the three samples. The sp^2 hybridized carbon of the aromatic ring (C in C–N–C) at 288 eV was the most abundant configuration at about 87% for the three samples. N 1 s core level spectra displayed the three characteristic peaks for g-C_3N_4 at binding energies of 398.5, 399.7 and 400.9 ascribed to the sp^2 hybridized pyridine nitrogen in triazine rings (C=N–C), tertiary nitrogen N–$(C)_3$, and sp^3 terminal N (C–N–H), respectively (Fig. 3b). Satellite peaks are observed at binding energies of 404, 406.6 and 411.4 eV as summarized in Table S3 [18]. The wide scans, high resolution C 1 s (Fig. 3a, Table S2) and N 1 s (Fig. 3b, Table S3) spectra of the samples are generally similar, confirming that the g-C_3N_4 structure is maintained even in the 3D g-C_3N_4 samples.

The efficient photocatalytic activity of 3D g-C_3N_4 is demonstrated

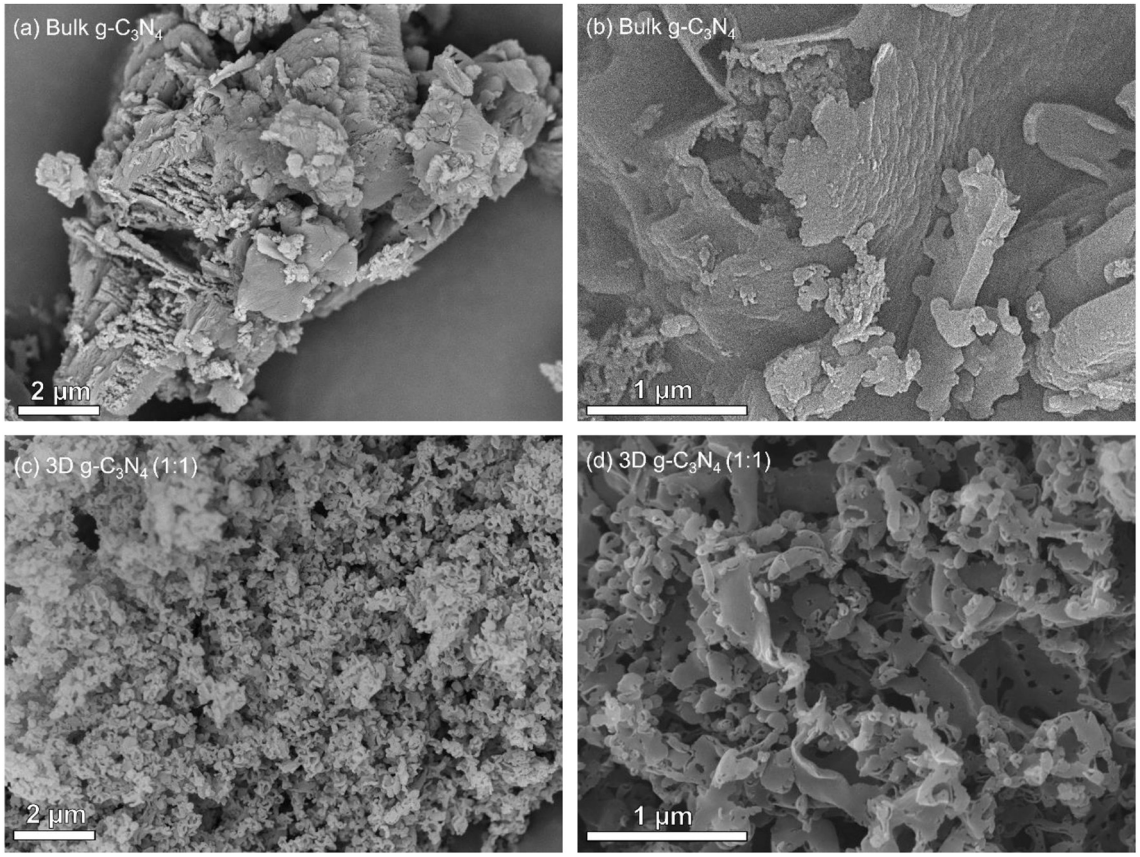

Fig. 2. In Beam SEM images of (a) bulk g-C_3N_4, 5 kV, 30 kx, (b) bulk g-C_3N_4, 15 kV, 120 kx, (c) 3D g-C_3N_4 (1:1), 5 kV. 30 kx and (d) 3D g-C_3N_4 (1:1), 15 kV, 120 kx.

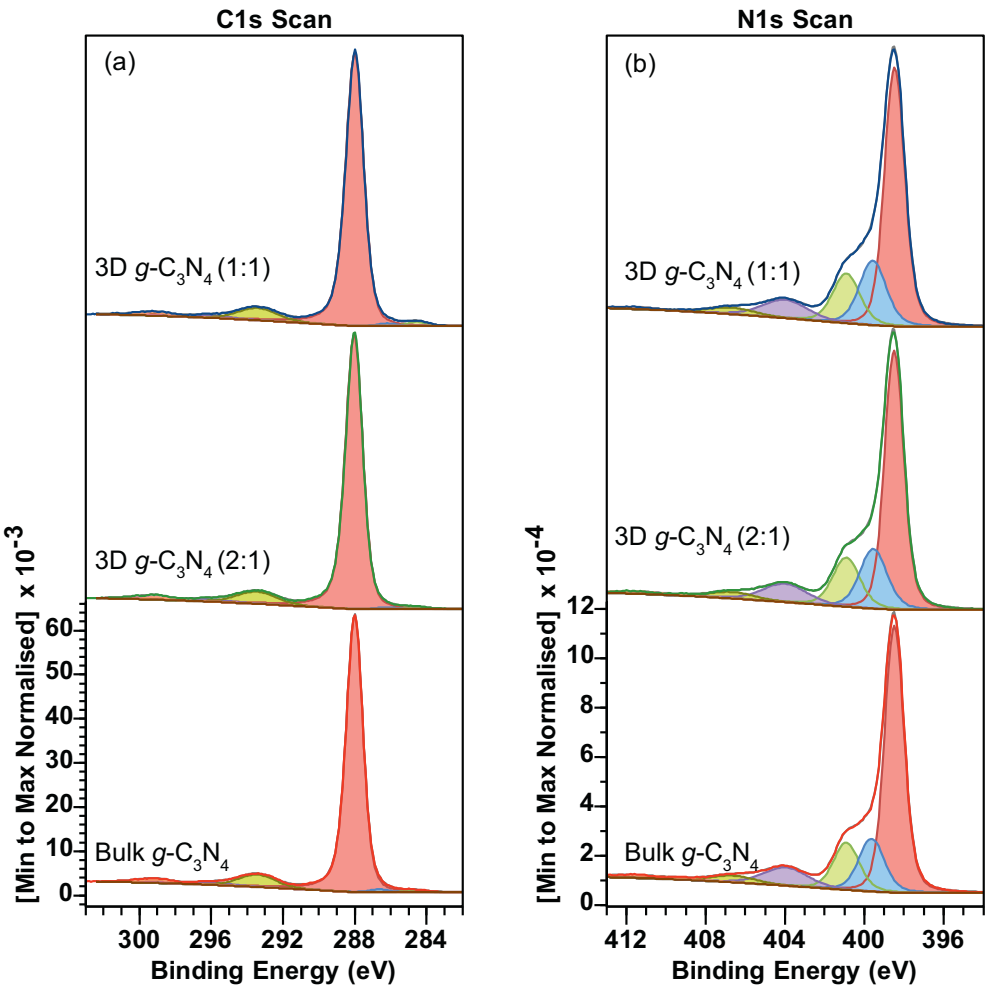

Fig. 3. High resolution (a) C 1 s and (b) N 1 s spectra for the different samples, bulk g-C_3N_4, 3D g-C_3N_4 (2:1) and 3D g-C_3N_4 (1:1) as indicated.

through phenol degradation, bulk *g*-C_3N_4 has also been analysed under similar conditions for comparison as shown in Fig. 4a. Bulk *g*-C_3N_4 displays a 73% phenol degradation efficiency when tested in chloride-free solutions, meanwhile 3D *g*-C_3N_4 (2:1) shows enhanced phenol removal efficiency with 80% achieved after 240 min of reaction. The porous graphitic carbon nitride sample prepared using equivalent mol ratios of melamine and cyanuric acid [3D *g*-C_3N_4 (1:1)] further enhanced phenol degradation up to 99%. It is evident that the improved properties of the 3D *g*-C_3N_4 had a favourable impact on the phenol removal efficiency even though XPS showed similar surface chemistry for all the materials. The observed phenol degradation rate constants (k_1) for the 3D *g*-C_3N_4 (1:1) and 3D *g*-C_3N_4 (2:1) were 8.1×10^{-3} and 6.0×10^{-3} and were higher than bulk *g*-C_3N_4 as shown in Fig. 4b and Table 1. k_1 values were determined from the linear range of eq. (1), where C_0 and C_i are the phenol concentrations at $t = 0$ and $t = i$, given (i = 0, 15, 30, 60, 90, 120, 180, 240) [20,21].

$$ln\left(\frac{C_0}{C_i}\right) = kt \tag{1}$$

The phenol degradation capability of 3D *g*-C_3N_4 in hypersaline brine solutions was evaluated using [Cl^-] = 100 g/L. Chloride concentration in our simulated brine experiments were determined from reported maximum levels in shale gas extraction operations [22–24] but incorporating a dilution factor of 2. Larger dilution factors (lower chloride concentrations) are usually not practical in a typical produced water reservoir due to large effluent quantities. Photocatalytic phenol degradation decreased when experiments were performed in brine solutions (Fig. 4c-d). Bulk *g*-C_3N_4 achieved a 47% phenol removal efficiency in brines, but 3D *g*-C_3N_4 (1:1) enhanced the degradation slightly to 58% (Fig. 4d) corresponding to rate constants of 2.6×10^{-3} and 3.7×10^{-3}, respectively. The decrease in photocatalytic activity in brines is attributed to the blockage of valence band holes and the scavenging of photogenerated radicals by the excess Cl^- ions [20,25,26]. Notably, photodegradation of phenol still proceeded in brines and was enhanced over the 3D *g*-C_3N_4 photocatalysts relative to bulk *g*-C_3N_4.

Fig. S3 displays spectral monitoring of phenol degradation in brines vs chloride free solutions using 3D *g*-C_3N_4 (1:1) as a photocatalyst. Phenol peaks at 210 and 270 nm decreased with illumination time indicating a decrease in concentration of the model organic compound as it was converted to carbon dioxide, water and other reaction intermediates. Phenol degradation was inhibited in brines with strong phenol signals still detected after 240 min (Fig. S3b), in agreement with HPLC results discussed above.

4. Conclusion

In summary, we used a molecular self-assembly approach to prepare porous 3D *g*-C_3N_4 and tested the resulting materials as photocatalysts for the decomposition of phenol in aqueous solutions. Characterisation of the prepared 3D *g*-C_3N_4 by XRD and XPS showed that it had similar chemical compositions to nonporous bulk *g*-C_3N_4. In addition, similar band gap energies in the range 2.72–2.79 eV were measured. The porous structure of 3D *g*-C_3N_4 was evident from N_2 sorption measurements and microscopic analysis by SEM. In the absence of brines, phenol

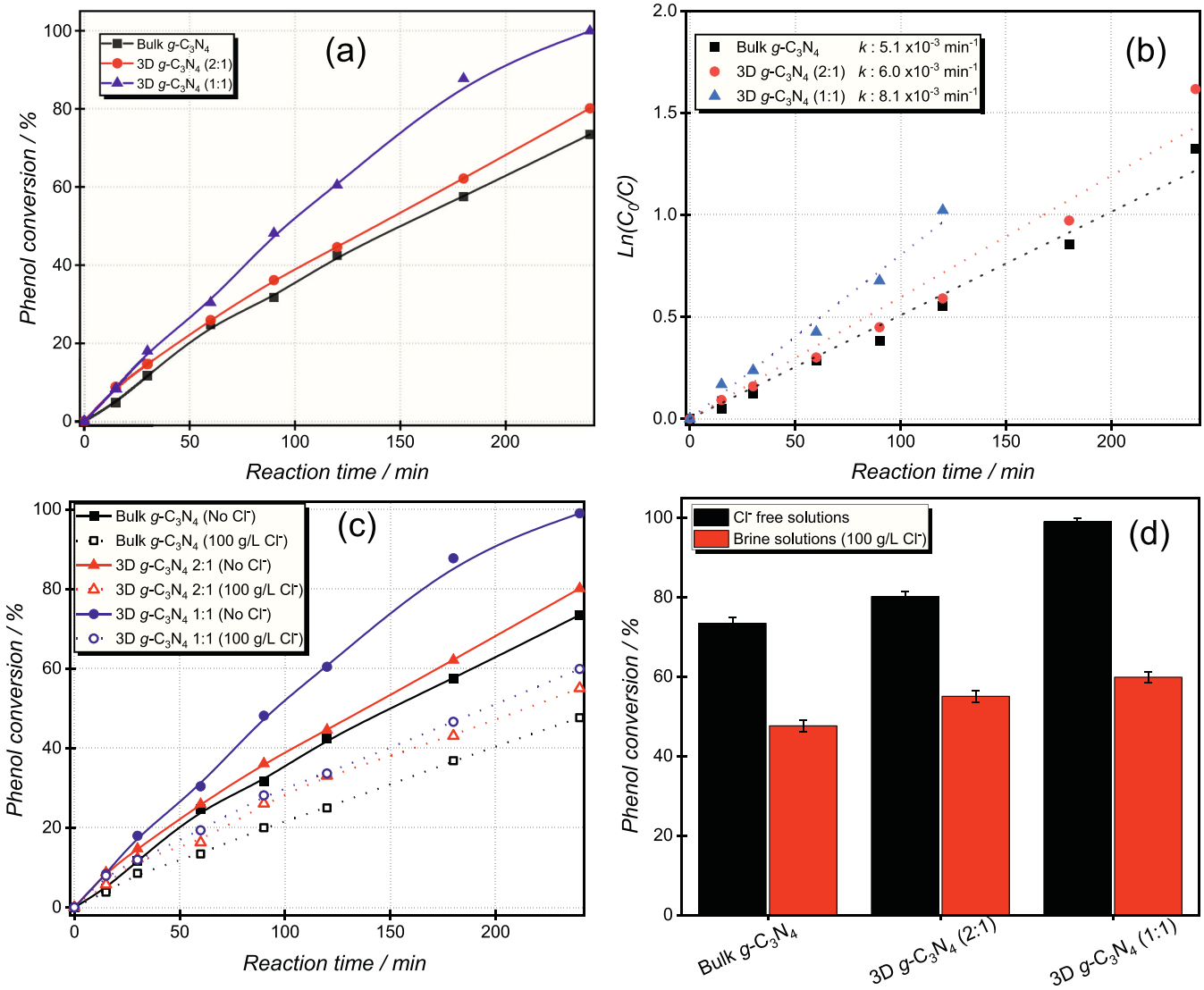

Fig. 4. (a) Phenol conversions over different g-C_3N_4 samples in chloride-free solutions as determined by HPLC, (b) corresponding pseudo-first-order rate constants, (c) effect of brines on photo-activity and, (d) summarized 240 min phenol conversions measured in brines and chloride-free solutions.

Table 1
Summary of the textual and catalytic results, SA, PV, PS and Eg of the samples.

Sample	SA_{BET}[a] (m^2/g)	P_V[b] (cm^3/g)	P_S[c] (nm)	Eg[d] (eV)	k_1 (min^{-1})[e]	k_2 (min^{-1})[f]
Bulk g-C_3N_4	10	0.11	2.0	2.72	5.1×10^{-3}	2.6×10^{-3}
3D g-C_3N_4 (2:1)	59	0.20	2.1	2.78	6.0×10^{-3}	3.3×10^{-3}
3D g-C_3N_4 (1:1)	87	0.48	3.0	2.79	8.1×10^{-3}	3.7×10^{-3}

[a] surface area
[b] Pore volume.
[c] Pore size.
[d] band gap.
[e] Pseudo-first-order rate constant (chloride-free solutions).
[f] Pseudo-first-order rate constant (measured in brines).

degradation proceeded quickly over the samples with 3D g-C_3N_4 achieving complete conversion of phenol within 240 min. The enhanced photo-activity over 3D g-C_3N_4 relative to bulk g-C_3N_4 is attributed to the accessibility of additional active sites on the porous material and reduced recombination of charge carriers due to the 3D structure. The activity of the photocatalysts was noted to decline in brine solutions even though it still proceeded appreciably. In all investigated scenarios 3D g-C_3N_4 displayed enhanced photocatalytic activity relative to bulk g-C_3N_4.

Credit authors statement

G.J.H., P.R.D., S.P., M.W.D. conceptualization of the study and formal analysis; G.J.H., P.R.D. supervision and funding acquisition; M.W.D. conducted experiments and data curation; T.E.D. and D.J.M. performed catalyst characterisation and corresponding data processing; M.W.D. wrote the original draft and supporting information. All the authors discussed the results and contributed to the work.

Declaration of Competing Interest

The authors declare that they have no known competing financial interests or personal relationships that could have appeared to influence the work reported in this paper.

Acknowledgements

This research was financially supported by Cardiff University and the UK Catalysis Hub through our membership of the UK Catalysis Hub Consortium, funded by the Engineering and Physical Sciences Research Council (EPSRC) (grants EP/K014706/1, EP/K014668/1, EP/K014854/1, EP/K014714/1, and EP/K014706/2). XP spectra were acquired by EPSRC National Facility for Photoelectron Spectroscopy (HarwellXPS), operated by Cardiff University and UCL under contract number PR16195.

Appendix A. Supplementary data

Supplementary data to this article can be found online at https://doi.org/10.1016/j.catcom.2022.106480.

References

[1] G. Zichittella, J. Pérez-Ramírez, Status and prospects of the decentralised valorisation of natural gas into energy and energy carriers, Chem. Soc. Rev. 50 (2021) 2984–3012.
[2] R.A. Kerr, Natural gas from shale bursts onto the scene, Science 328 (2010) 1624–1626.
[3] Q. Lyu, J. Tan, L. Li, Y. Ju, A. Busch, D.A. Wood, P.G. Ranjith, R. Middleton, B. Shu, C. Hu, Z. Wang, R. Hu, The role of supercritical carbon dioxide for recovery of shale gas and sequestration in gas shale reservoirs, Energy Environ. Sci. 14 (2021) 4203–4227.
[4] T.L.S. Silva, S. Morales-Torres, S. Castro-Silva, J.L. Figueiredo, A.M.T. Silva, An overview on exploration and environmental impact of unconventional gas sources and treatment options for produced water, J. Environ. Manag. 200 (2017) 511–529.
[5] Y. Hu, P. Zhang, J. Du, C. Kim, S. Han, W. Choi, Bifunctional carbon nitride exhibiting both enhanced photoactivity and residual catalytic activity in the post-irradiation dark period, ACS Catal. 11 (2021) 14941–14955.
[6] H. Wang, S. Jiang, S. Chen, D. Li, X. Zhang, W. Shao, X. Sun, J. Xie, Z. Zhao, Q. Zhang, Y. Tian, Y. Xie, Enhanced singlet oxygen generation in oxidized graphitic carbon nitride for organic synthesis, Adv. Mater. 28 (2016) 6940–6945.
[7] J. Kim, H. Lee, J.-Y. Lee, K.-H. Park, W. Kim, J.H. Lee, H.-J. Kang, S.W. Hong, H.-J. Park, S. Lee, J.-H. Lee, H.-D. Park, J.Y. Kim, Y.W. Jeong, J. Lee, Photosensitized production of singlet oxygen via C60 fullerene covalently attached to functionalized silica-coated stainless-steel mesh: remote bacterial and viral inactivation, Appl. Catal. B Environ. 270 (2020), 118862.
[8] A. Kashyap, E. Ramasamy, V. Ramalingam, M. Pattabiraman, Supramolecular control of singlet oxygen generation, Molecules 26 (2021) 2673.
[9] L. Kong, J. Wang, X. Mu, R. Li, X. Li, X. Fan, P. Song, F. Ma, M. Sun, Porous size dependent g-C3N4 for efficient photocatalysts: regulation synthesizes and physical mechanism, materials today, Energy 13 (2019) 11–21.
[10] X. Chen, R. Shi, Q. Chen, Z. Zhang, W. Jiang, Y. Zhu, T. Zhang, Three-dimensional porous g-C3N4 for highly efficient photocatalytic overall water splitting, Nano Energy 59 (2019) 644–650.
[11] M. Shalom, S. Inal, C. Fettkenhauer, D. Neher, M. Antonietti, Improving carbon nitride Photocatalysis by supramolecular preorganization of monomers, J. Am. Chem. Soc. 135 (2013) 7118–7121.
[12] N. Fairley, V. Fernandez, M. Richard-Plouet, C. Guillot-Deudon, J. Walton, E. Smith, D. Flahaut, M. Greiner, M. Biesinger, S. Tougaard, D. Morgan, J. Baltrusaitis, Systematic and collaborative approach to problem solving using X-ray photoelectron spectroscopy, Appl.Surf. Sci. Adv. 5 (2021), 100112.
[13] C. Zhao, C. Shi, Q. Li, X. Wang, G. Zeng, S. Ye, B. Jiang, J. Liu, Nitrogen vacancy-rich porous carbon nitride nanosheets for efficient photocatalytic H2O2 production, Mater. Today Energy 24 (2022), 100926.
[14] K. Wang, H. Wang, Q. Cheng, C. Gao, G. Wang, X. Wu, Molecular-functionalized engineering of porous carbon nitride nanosheets for wide-spectrum responsive solar fuel generation, J. Colloid Interface Sci. 607 (2022) 1061–1070.
[15] P. Xia, S. Cao, B. Zhu, M. Liu, M. Shi, J. Yu, Y. Zhang, Designing a 0D/2D S-scheme heterojunction over polymeric carbon nitride for visible-light photocatalytic inactivation of Bacteria, Angew. Chem. Int. Ed. 59 (2020) 5218–5225.
[16] Y.-H. Li, J.-Y. Li, Y.-J. Xu, Bimetallic nanoparticles as cocatalysts for versatile photoredox catalysis, EnergyChem 3 (2021), 100047.
[17] K.-Q. Lu, X. Xin, N. Zhang, Z.-R. Tang, Y.-J. Xu, Photoredox catalysis over graphene aerogel-supported composites, J. Mater. Chem. A 6 (2018) 4590–4604.
[18] D.J. Morgan, Core-level reference spectra for bulk graphitic carbon nitride (g-C3N4), Surface Sci. Spectra 28 (2021), 014007.
[19] G. Filippini, F. Longobardo, L. Forster, A. Criado, G.D. Carmine, L. Nasi, C. D'Agostino, M. Melchionna, P. Fornasiero, M. Prato, Light-driven, heterogeneous organocatalysts for C–C bond formation toward valuable perfluoroalkylated intermediates, Sci. Adv. 6 (2020) eabc9923.
[20] X. Yu, Y. Lin, H. Liu, C. Yang, Y. Peng, C. Du, S. Wu, X. Li, Y. Zhong, Photocatalytic performances of heterojunction catalysts of silver phosphate modified by PANI and Cr-doped SrTiO3 for organic pollutant removal from high salinity wastewater, J. Colloid Interface Sci. 561 (2020) 379–395.
[21] Z. Dong, R. Zhou, L. Xiong, H. Li, Q. Liu, L. Zheng, Z. Guo, Z. Deng, Preparation of a Ti0.7W0.3O2/TiO2 nanocomposite interfacial photocatalyst and its photocatalytic degradation of phenol pollutants in wastewater, nanoscale, Advances 2 (2020) 425–437.
[22] A.J. Kondash, N.E. Lauer, A. Vengosh, The intensification of the water footprint of hydraulic fracturing, Sci. Adv. 4 (2018) eaar5982.
[23] A. Butkovskyi, H. Bruning, S.A.E. Kools, H.H.M. Rijnaarts, A.P. Van Wezel, Organic pollutants in shale gas flowback and produced waters: identification, potential ecological impact, and implications for treatment strategies, Environ. Sci. Technol. 51 (2017) 4740–4754.
[24] C. Danforth, W.A. Chiu, I. Rusyn, K. Schultz, A. Bolden, C. Kwiatkowski, E. Craft, An integrative method for identification and prioritization of constituents of concern in produced water from onshore oil and gas extraction, Environ. Int. 134 (2020), 105280.
[25] E. Bouleghlimat, D. Bethell, P.R. Davies, The photocatalytic destruction of cinnamic acid and cinnamyl alcohol: mechanism and the effect of aqueous ions, Chemosphere 251 (2020), 126469.
[26] Z. Wang, P. Feng, H. Chen, Q. Yu, Photocatalytic performance and dispersion stability of nanodispersed TiO(2) hydrosol in electrolyte solutions with different cations, J. Environ. Sci. (China) 88 (2020) 59–71.